Computational Screening of *p*-Type Transparent Conducting Oxides Using the Optical Absorption Spectra and Oxygen-Vacancy Formation Energies

Yu Kumagai

Phys. Rev. Applied **19**, 034063 — Published 20 March 2023

DOI: 10.1103/PhysRevApplied.19.034063

Computational screening of *p*-type transparent conducting oxides using the optical absorption spectra and oxygen-vacancy formation energies

Yu Kumagai*

Institute for Materials Research, Tohoku University, 2-1-1 Katahira, Aoba-ku, Sendai, 980-8577, Japan

* yukumagai@tohoku.ac.jp

Although *n*-type transparent conducting oxides (TCOs) with visible-light transparency and electric conductivity have been used in industry for decades, the *p*-type counterparts have not been commercialized. To search for promising *p*-type TCOs, computational screening has been applied by several research groups in the last decade. However, screening of a wide material space was mainly based on the approximated physical quantities, such as underestimated band gaps, and band-alignment techniques. In particular, it is unlikely that the band alignments can predict the dopability in a wide range of insulators because they do not include information about the chemical potentials of the constituent elements. In this study, we used the optical absorption spectra calculated with dielectric-dependent hybrid functionals and the formation energies of oxygen vacancies as screening parameters. Oxygen vacancies are known to act as hole killers when seeking for *p*-type TCOs, and indeed only 156 out of the 845 oxides were found to have benign oxygen vacancies for *p*-type doping. As a result, we identified six potential *p*-type TCOs from 845 oxides: Na_3AgO_2, $Rb_2Pb_2O_3$, $Cs_2Pb_2O_3$, CsCuO, $K_2Pb_2O_3$, and B_6O. Na_3AgO_2, $Rb_2Pb_2O_3$, and

$Cs_2Pb_2O_3$ are identified potential *p*-type TCOs, while CsCuO, $K_2Pb_2O_3$, and B_6O have been previously proposed. By analyzing the electronic structures and point-defect properties of Na_3AgO_2, CsCuO, and $K_2Pb_2O_3$ in detail, we found that they show *p*-type conductivity even without external doping, which validates the use of the formation energies of oxygen vacancies as descriptors of the *p*-type dopability of oxides.

I. INTRODUCTION

Transparent conductors (TCs) that show both visible-light transparency and electric conductivity can be used for various applications, such as transparent thin-film transistors, touch panel displays, and photovoltaic cells [1,2]. Because of the incompatibility between transparency and electric conductivity, only a limited number of TCs have been discovered. After many years of research, Sn-doped In_2O_3 has become the representative *n*-type transparent conducting oxide (TCO), and it has been commercially used for decades [3]. Amorphous indium gallium zinc oxide has also recently been used because of its high mobility at low processing temperatures, relatively low fabrication cost, and good transparency [4].

The performance of the *p*-type TCOs is not sufficiently high for them to be commercialized. Oxides are a promising class of *p*-type TCs because they tend to have relatively wide band gaps and to be easily synthesized under atmospheric conditions [5,6]. Furthermore, the heterojunction between oxides is desirable to suppress oxygen-related defect states at the interface. The problem is that *p*-type doping in oxides is usually difficult because the energy levels of the O-2*p* bands are too deep to introduce hole carriers. In 1997, Kawazoe et al. proposed that oxides are *p*-type dopable when the valence band is pushed up by hybridizing the O-2*p* bands with cationic orbitals whose levels are comparable with those of the O-2*p* orbitals [7]. They demonstrated the strategy with $CuAlO_2$, in which the Cu-3*d* orbitals hybridize with the O-2*p* orbitals.

After the discovery of $CuAlO_2$, several candidates for *p*-type TCOs have been proposed [5], and their computational screening has flourished in the last decade [8–15]. For example, Hautier et al. [8] reported extensive screening of *p*-type TCOs from thousands of oxides in 2013. In their study, the candidates were initially screened based on the hole effective masses and band gaps calculated using the Perdew–Burke–Ernzerhof (PBE) generalized-gradient approximation [16]. For the screened oxides, they calculated more accurate band gaps with the one-shot GW approximation (G_0W_0) [17] and vacancy formation energies with PBE. Similar high-throughput first-principles screening has also been performed for compounds other than oxides, such as phosphides and sulfides [10,11].

P-type TCOs should be screened in view of the optical transparency and electric conductivity. In computational studies, the transparency is mostly approximated by the minimum direct band gap in the reciprocal space. However, the optical gaps are much larger than those when the band-edge transitions are dipole prohibited. In fact, the minimum direct transitions in many TCOs are dipole forbidden, including in In_2O_3 [18], SnO_2 [19], and $CuAlO_2$ [20]. It is therefore more desirable to use the optical absorption spectrum as a screening criterion.

The band gaps used for initial screening are mostly calculated using semilocal functionals, such as the PBE functional [16], which usually greatly underestimates the band gaps. The problem is not the underestimation, but that the trend is not consistent. For example, the PBE band gap of ZnO is 0.73 eV, as reported in the Materials Project, [21] which is only 22% of the experimental value of 3.3 eV [22]. In contrast, the PBE band gap of monoclinic HfO_2 is 4.0 eV, which is 70% of the experimental band gap of 5.7 eV [23]. Such large uncertainty will increase the numbers of false positives and false negatives in the screened candidates and excluded materials, respectively.

The electric conductivity σ can be expressed as

$$\sigma = en\mu = e^2 n \frac{\tau}{m^*} \quad (1),$$

where e is the elementary charge, μ is the mobility (=$e\tau/m^*$), n is the carrier concentration, τ is the average diffusion time, and m^* is the effective mass [24]. τ is generally difficult to calculate from first principles. Although novel computational methods have been proposed recently [25], it is still not easy to perform their high-throughput calculations. Thus, it is not explicitly considered in computational screening. Conversely, m^* is easily evaluated from the band structure or density of state (DOS). All of the best n-type TCOs show very low electron effective masses, which legitimates the use of the effective mass as a criterion [8].

In addition to μ, the feasibility of p-type doping that is related to the carrier concentration is a key factor, because it is not easily realized in oxides, as mentioned above. The p-type doping necessitates acceptor-type native defects and/or dopants with small formation energies. In addition, the donor-type defects that annihilate holes, or so-called "hole killers" should be suppressed and have larger formation energies at the Fermi level located near the valence band maximum (VBM) [26]. Although the importance of the defect properties has been emphasized in previous screening studies [8,9,14], it is generally cumbersome and computationally demanding to calculate the energies of point defects from first principles. Therefore, in the initial screening phase, the dopability is determined using more easily calculated band alignments. Some studies have used the branch point energies [11,14], but their prediction capability is questionable [9,11]. Yim et al.

proposed to use the hydrogen impurity energy as a descriptor, which is shown to successfully distinguish established *p*- and *n*-type TCOs [9]. However, this technique is also considered an alternative band alignment technique because it determines the position of the VBM with respect to the reference level at the constant H chemical potential (e.g., the H_2 molecule energy).

The chemical potentials of the constituent elements are controllable as long as the host material is stable with respect to the competing phases, and they are directly related to the defect formation energies. For example, when the O chemical potential is decreased by 1 eV, the concentration of oxygen vacancies (V_O) is increased by a factor of 10^5 at a typical sintering temperature 1273K. However, the aforementioned alignment techniques do not, in principle, include information about the chemical potentials unfortunately. Therefore, it is desirable to use defect formation energies even in the initial screening while taking into account the chemical potentials. Based on the previous theoretical studies on point defects in oxides such as ZnO [26], In_2O_3 [27], SnO_2 [27], $BaTiO_3$ [28], $SrTiO_3$ [29], V_O are typical native defects and tend to act as main hole killers.

In this study, we screened 845 oxides for potential *p*-type TCOs using the physical properties directly linked to the transparency (optical absorption spectra) and conductivity (oxygen-vacancy formation energies and effective masses). The band structures, effective masses, and optical absorption spectra were calculated, while we used our previous high-throughput calculations of V_O [30] for screening of the *p*-type dopability. For the first-principles calculations, we used dielectric-dependent (dd) hybrid functionals, which can accurately predict band gaps [31].

The screening identified six potential *p*-type TCOs: Na_3AgO_2, $Rb_2Pb_2O_3$, $Cs_2Pb_2O_3$, CsCuO, $K_2Pb_2O_3$, and B_6O. Na_3AgO_2 was identified to be a potential *p*-type TCO, while CsCuO [9], $K_2Pb_2O_3$ [8], and B_6O [8] have been previously identified. $Rb_2Pb_2O_3$ and $Cs_2Pb_2O_3$ were also identified as potential TCOs although they are related compounds to $K_2Pb_2O_3$. For Na_3AgO_2, CsCuO, and $K_2Pb_2O_3$, we calculated not only the vacancies, but also the antisites and interstitials using the dd hybrid functionals. We found that they are indeed p-type semiconductors even without external doping. However, it is found that Na_3AgO_2 and CsCuO exhibits the one-dimensional (1D) or small polaronic state, which would lead to anisotropic or small conductivity, respectively. On the other hand, $K_2Pb_2O_3$ acts as a p-type semiconductor with moderate carrier concentration, and it can be enhanced via Na doping.

II. Computational methods

A. Computational settings of first-principles calculations

The first-principles calculations were performed using the projector augmented-wave (PAW) method [32,33] implemented in the Vienna Ab initio Simulation Package (VASP) [34]. We used the same PAW data sets as those used in our previous study [30]. To use the oxygen-vacancy formation energies ($E_\mathrm{f}[V_\mathrm{O}]$) calculated in our previous study [30], we targeted 845 oxides for which all of the inequivalent oxygen vacancies were successfully finished. In these calculations, three charge states (0, +1, and +2) were considered for oxygen vacancies. The unit cells relaxed with the PBEsol functional [35] were used for the high-throughput calculations in this study.

The calculations of the band structures and optical absorption spectra were performed using the dd hybrid functionals [31] in which the exchange–correlation (XC) interactions are evaluated by

$$v_\mathrm{XC}(\boldsymbol{r},\boldsymbol{r}') = a v_\mathrm{X}^{nl}(\boldsymbol{r},\boldsymbol{r}') + (1-a) v_\mathrm{X}^{l}(\boldsymbol{r}) + v_\mathrm{C}^{l}(\boldsymbol{r}) \quad (2),$$

where $v_\mathrm{X}^{nl}(\boldsymbol{r},\boldsymbol{r}')$ and $v_\mathrm{X}^{l}(\boldsymbol{r})$ are the nonlocal and (semi)local exchange potentials, respectively. $v_\mathrm{C}^{l}(\boldsymbol{r})$ is a correlation potential estimated from a (semi)local potential. The mixing parameter for an exchange potential is determined by $a = \langle \varepsilon_{\mathrm{ele}} \rangle^{-1}$, where $\langle \varepsilon_{\mathrm{ele}} \rangle$ is the spherically averaged ion-clamped dielectric constant. The $\langle \varepsilon_{\mathrm{ele}} \rangle$ values were also taken from our previous study [30], in which the dielectric constants were calculated using the PBEsol functional with Hubbard U corrections [36] for the Cu- and Zn-3*d* orbitals and Ce-4*f* orbitals with $U_{\mathrm{eff}} = 5$ eV (PBEsol(+U)). We used PBEsol [35] for $v_{\mathrm{X}}^{l}(\boldsymbol{r})$ and $v_{\mathrm{C}}^{l}(\boldsymbol{r})$ in Eq. (2).

For the band-structure calculations of the 845 oxides and some screened oxides, the *k*-point sampling densities were set to 2.5 and 3.5 Å^{-1}, and the band paths were determined using seekpath [37] with mesh distances of 0.025 and 0.015 Å^{-1}, respectively. When calculating the dielectric functions, the *k*-point density was doubled along all of the reciprocal axes and the *k*-point meshes were centered at the Γ point for sampling the special points at the zone boundaries. To reduce the computational time, the *k*-point sampling for the exact exchange potential was reduced to half in all of the directions.

To calculate the optical absorption spectra, we first obtained the imaginary parts of the dielectric functions ϵ_1. The real parts ϵ_2 were then calculated using the Kramers–Kronig transformation with a complex shift of 0.01 eV. We next estimated their spherical averages $\bar{\epsilon}_1$ and $\bar{\epsilon}_2$, and the optical absorption spectra:

$$\alpha = \frac{4\pi}{\lambda}\sqrt{\frac{1}{2}\left(-\bar{\epsilon}_1 + \sqrt{(\bar{\epsilon}_1^2 + \bar{\epsilon}_2^2)}\right)}, \quad (3)$$

where λ is the wavelength [38]. When strong absorption is allowed near the band edges, the absorption spectrum shows a steep increase to >10^4 cm^{-1} just above the band gap. Therefore, we define the optical gaps as the energies at which the absorption spectra first reach 10^4 cm^{-1}.

The band-averaged effective mass tensors and DOS were also evaluated based on the calculations of the dielectric functions. The former were calculated using BoltzTraP2 [38], where the carrier concentration and temperature were set to 10^{16} cm^{-3} and 300 K, respectively. The minima of the effective hole masses m_h^* were determined by diagonalizing the effective mass tensors.

All of the VASP input settings were generated using the VISE code (version 0.6.6) [39]. Automation of the first-principles calculations was performed with fireworks [40], pymatgen [41], and custodian [41].

B. Modeling of the point defects

For the oxygen vacancies calculations in our previous study [30], we adopted the PBEsol functional with Hubbard *U* corrections with the same parameters in this study. The band-edge positions were then determined using the non-self-consistent dd hybrid functional [42].

In this study, the self-consistent dd hybrid functionals were used to calculate the point defects in Na_3AgO_2, CsCuO, and $K_2Pb_2O_3$. The Fock exchange mixing parameters are given in Table 1. The lattice constants and internal coordinates in the perfect structures were fully relaxed for each mixing parameter. We constructed nearly isotropic supercells by expanding the conventional unit cells. The numbers of atoms in the supercells were 96, 288, and 224 for Na_3AgO_2, CsCuO, and $K_2Pb_2O_3$, respectively. The reciprocal space of Na_3AgO_2 was sampled with a $2\times2\times1$ *k*-point grid, while CsCuO and $K_2Pb_2O_3$ were calculated with only the Γ point.

We modeled the vacancies at all the inequivalent sites, cation antisites, and interstitials. We placed the interstitial sites at the local minima of the all-electron charge densities in the perfect crystals, which were identified using scikit-image [43]. We also considered split-type vacancies/antisites at the Cu and Ag sites because the split-type Cu vacancy is known to be stable in Cu_2O [44]. To lower the initial site symmetries, atoms within 1.3 times the shortest bond length from the initial defect site were randomly displaced by up to 0.2 Å. The defect charge states were determined from the oxidation states. For example, because the oxidation states of K and Pb in $K_2Pb_2O_3$ are 1+ and 2+, we calculated the 0 and −1 charge states for the K_{Pb} antisites.

The calculations of the defect formation energies followed the general methodology. [45] The formation energy of a point defect is given by

$$E_{\mathrm{f}}[D^q] = \{E[D^q] - E_{\mathrm{corr}}[D^q]\} - E_{\mathrm{p}} + \textstyle\sum_i \Delta n_i\, \mu_i + q(\varepsilon_{\mathrm{VBM}} + \Delta\varepsilon_{\mathrm{F}}), \quad (4)$$

where $E[D^q]$ and E_{p} are the total energies of the supercell with defect D in charge state q and the perfect crystal supercell without defects, respectively. n_i is the number of i-type atoms removed ($n_i < 0$) or added ($n_i > 0$), and μ_i is its chemical potential. $\varepsilon_{\mathrm{VBM}}$ is the energy level of the VBM, while $\Delta\varepsilon_{\mathrm{F}}$ is the Fermi level with respect to the VBM. $E_{\mathrm{corr}}[D^q]$ is a correction energy for the finite size error. It was estimated using the extended Freysoldt–Neugebauer–Van de Walle scheme [46,47], which works satisfactorily for various systems [28,48–53]. Note that this correction technique was also applied to the oxygen vacancy formation energies [30], which are used in this study. The dielectric constants were then defined as the sum of the ion-clamped and ionic dielectric constants. The former were evaluated using the dd hybrid functional, while the latter were taken from our previous study using the PBEsol(+*U*) functional [30]. The identification of the perturbed host states was performed according to our previously reported method [30].

We constructed the chemical potential diagrams from the total energies of the competing phases including the impurity phases calculated using the same exact exchange mixing parameter for each oxide. The standard state of oxygen was set to the O_2 molecule. The competing phase lists were taken from the Materials Project Database (MPD) [21]. When using the oxygen vacancy formation energies in our previous study, the chemical potentials were determined from the MPD, where the total energies are empirically corrected [30,54].

The defect and carrier concentrations were evaluated from the Boltzmann and the Fermi-Dirac distributions, respectively. Based on their concentrations and the charge neutrality condition, the Fermi level is finally determined (see *e.g.* [49] for details). When calculating the carrier concentration at room temperature, we assume that the defects are created at the sintering temperatures but the defect concentrations are kept fixed during quenching while their charge states are variable.

All defect related processes were performed with pydefect [55].

III. Results

A. Screening of *p*-type TCOs

To achieve *p*-type doping, the native donor-type defects that compensate for the carrier holes must be suppressed. Although oxygen vacancies are ubiquitous in oxides, only positively charged oxygen vacancies act as hole killers. Because the Fermi level is close to the VBM in *p*-type semiconductors, the energy of the positively charged oxygen vacancy at $\Delta\varepsilon_F = 0$ is an indicator of whether oxides are *p*-type dopable. In particular, when positively charged oxygen vacancies have negative $E_f[V_O]$ at $\Delta\varepsilon_F = 0$, the Fermi-level pinning occurs within the band gap, from which $\Delta\varepsilon_F$ cannot be lowered even with acceptor doping [56].

It is well known that, although considerable efforts have been made to realize the *p*-type ZnO, only limited success has been reported [57]. Since $E_f[V_O]$ at the O-rich condition in ZnO is close to zero, we use $E_f[V_O] = 0$ eV at $\Delta\varepsilon_F = 0$ as the baseline for the *p*-type dopability and classify the oxygen vacancies into three types.

- Type 1: Stable only in the neutral charge state regardless of $\Delta\varepsilon_F$ in the band gap (e.g., V_{O1} and V_{O2} in Fig. 1).
- Type 2: Positively charged but $E_f[V_O] > 0$ eV at $\Delta\varepsilon_F = 0$ (e.g., V_{O3}).
- Type 3: Positively charged but $E_f[V_O] \leq 0$ eV at $\Delta\varepsilon_F = 0$ (e.g., V_{O4}). The Fermi level where $E_f[V_O]$ becomes zero corresponds to a pinning level, from which $\Delta\varepsilon_F$ cannot be lowered even with acceptor doping.

In this study, we assumed that the chemical potentials are controllable within the stable region in the chemical potential diagram, and we considered O-rich conditions where oxygen vacancies are most suppressed.

The oxides without type-3 oxygen vacancies are good candidates for *p*-type TCOs because the oxygen vacancies are not dominant hole killers. We have therefore classified the oxides according to whether they have type-3 oxygen vacancies.

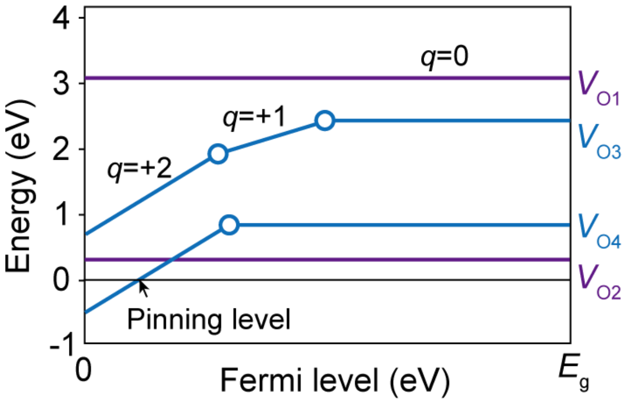

Figure 1. Schematic representation of the formation energies of the oxygen vacancies (V_O) with the charge states (q). The transition levels are indicated by circles.

The inverse of m_h^* as a function of the optical gap is shown in Fig. 2(a). Note that the mobility is inversely proportional to the effective mass (Eq. (1)). In some studies, the average hole effective mass has been used as a screening parameter, assuming the application of the polycrystals. We used the minimum effective mass because the crystal orientation can be controlled by adjusting the substrate and/or growth conditions. It is worth noting that as the optical gap increases, m_h^* tends to increase in Fig. 2(a). This is partly because the hybridization between the valence and conduction bands generally decreases as the band gap increases, resulting in a less dispersive band structure.

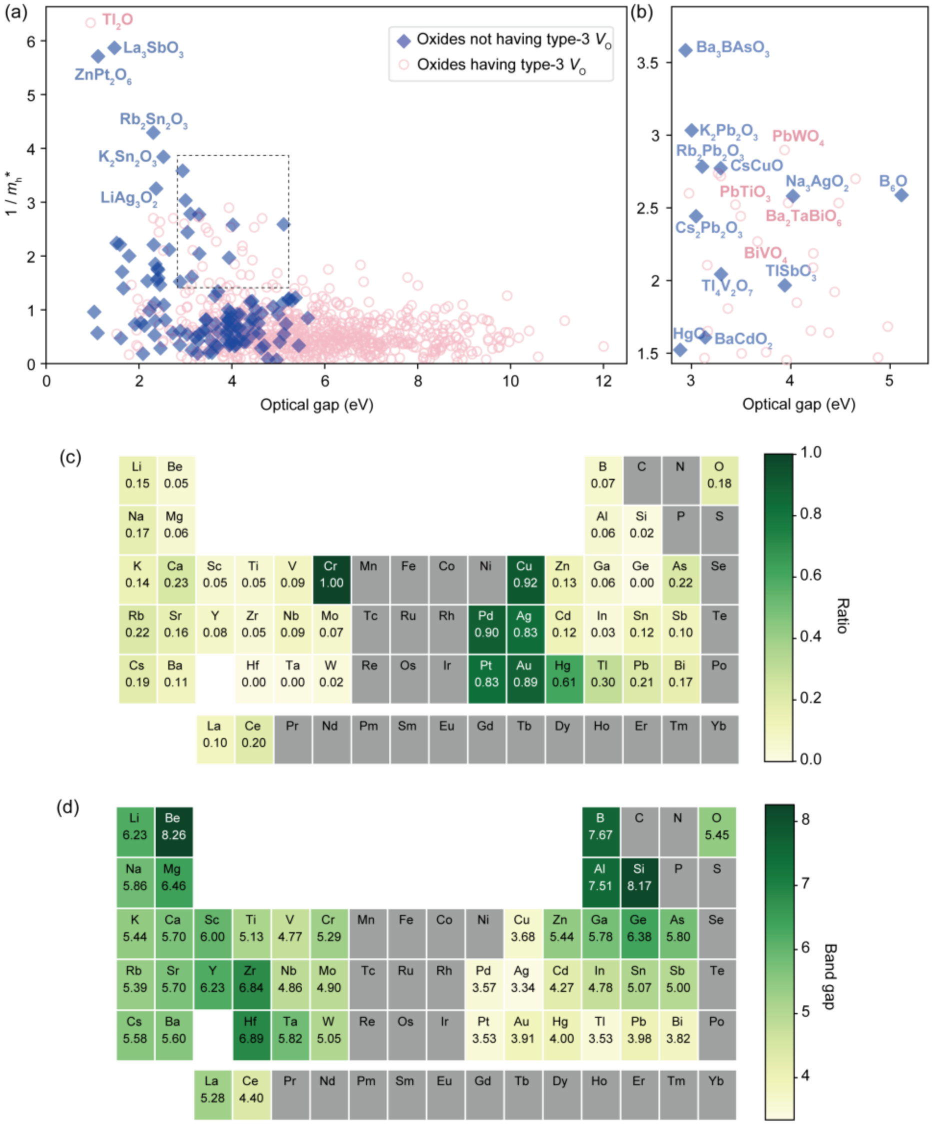

(c)

Li 0.15	Be 0.05											B 0.07	C	N	O 0.18
Na 0.17	Mg 0.06											Al 0.06	Si 0.02	P	S
K 0.14	Ca 0.23	Sc 0.05	Ti 0.05	V 0.09	Cr 1.00	Mn	Fe	Co	Ni	Cu 0.92	Zn 0.13	Ga 0.06	Ge 0.00	As 0.22	Se
Rb 0.22	Sr 0.16	Y 0.08	Zr 0.05	Nb 0.09	Mo 0.07	Tc	Ru	Rh	Pd 0.90	Ag 0.83	Cd 0.12	In 0.03	Sn 0.12	Sb 0.10	Te
Cs 0.19	Ba 0.11		Hf 0.00	Ta 0.00	W 0.02	Re	Os	Ir	Pt 0.83	Au 0.89	Hg 0.61	Tl 0.30	Pb 0.21	Bi 0.17	Po
		La 0.10	Ce 0.20	Pr	Nd	Pm	Sm	Eu	Gd	Tb	Dy	Ho	Er	Tm	Yb

(d)

Li 6.23	Be 8.26											B 7.67	C	N	O 5.45
Na 5.86	Mg 6.46											Al 7.51	Si 8.17	P	S
K 5.44	Ca 5.70	Sc 6.00	Ti 5.13	V 4.77	Cr 5.29	Mn	Fe	Co	Ni	Cu 3.68	Zn 5.44	Ga 5.78	Ge 6.38	As 5.80	Se
Rb 5.39	Sr 5.70	Y 6.23	Zr 6.84	Nb 4.86	Mo 4.90	Tc	Ru	Rh	Pd 3.57	Ag 3.34	Cd 4.27	In 4.78	Sn 5.07	Sb 5.00	Te
Cs 5.58	Ba 5.60		Hf 6.89	Ta 5.82	W 5.05	Re	Os	Ir	Pt 3.53	Au 3.91	Hg 4.00	Tl 3.53	Pb 3.98	Bi 3.82	Po
		La 5.28	Ce 4.40	Pr	Nd	Pm	Sm	Eu	Gd	Tb	Dy	Ho	Er	Tm	Yb

Figure 2. (a) Plot of the reciprocal of the minimum effective hole mass (m_h^*) versus the optical gap. The oxides with and without type-3 oxygen vacancies are distinguished by symbols and colors (see the text for details). (b) Magnification of a dashed rectangle in (a). (c) Proportion of oxides with only type 1 and/or 2 oxygen vacancies and (d) averaged optical gap of the oxides for each element. Only results with five or more oxides containing each element are shown. Overall averages are shown at the O element.

From Fig. 2(c), which shows the proportion of oxides with only type 1 and/or 2 oxygen vacancies for each element, a clear elemental bias can be seen. The oxides mainly belong to the following three groups:

- Group A: The oxides of the elements with fully or partially filled *d* electrons in the valence bands. Examples are Pd, Pt, Cu, Ag, and Au oxides. The *p*-type dopability is attributed to their higher energy levels than the O-2*p* bands as proposed by Kawazoe et al [7].
- Group B: The oxides containing elements with lone pair electrons. Examples include Tl, Sn, Pb, As, Sb, and Bi oxides. Their *p*-type doping is more plausible because their lone-pair bands also tend to have higher energy levels than the O-2*p* bands. This idea is also a common strategy to achieve *p*-type doping in oxides, *e.g.*, SnO [58].
- Group C: The oxides of elements with empty *d*-orbitals near the band edges. Examples include Cr, Zr, and Re oxides. The d^0 orbitals form covalent bonds with O-2*p* orbitals, resulting in greater band dispersion with higher valence band maxima. This is less commonly considered for the *p*-type doping so far.

The exceptions that do not belong to the three groups are B_6O, $Ca_3(BO_3)_2$, $CaCdO_2$, Na_2ReO_3, $Sr_3(BO_3)_2$, and ZnO. Since ZnO and $CaCdO_2$ have filled *d* orbitals even though their energy levels are much lower than O-2*p*, they are placed in Group A in the broad sense. Therefore, the remaining exceptions are B_6O, $Ca_3(BO_3)_2$, and $Sr_3(BO_3)_2$, which results in the last group:

- Group D: Boron oxides in which the oxygens are closely bonded to the boron atoms, resulting in higher oxygen vacancy formation energies.

Although the optical gap should be larger than 3.1 eV for TCs [5], we used a slightly smaller criterion of 2.8 eV in anticipation of the error of the dd hybrid functionals (see Fig. S1 in the Supporting Information [59]). An enlarged view of the dashed rectangle in Fig. 2(a) is shown in Fig. 2(b), where the oxides have an optical gap larger than 2.8 eV. Smaller m_h^* is more desirable as long as transparency is achieved in the visible range. Only 156 out of the 845 oxides were found not to have type-3 oxygen vacancies. Such a small proportion is expected from the fact that p-type doping of oxides is generally difficult.

It is usually more desirable to suppress charged oxygen vacancies as much as possible to achieve the p-type dopability. Therefore, in the Supplementary Materials, we show the screening results with a looser condition of $E_f[V_O]$ = 1.0 eV. We find that the number of oxides with only type-1 and/or -2 oxygen vacancies decreases from 156 to 122. However, among the superior candidates in the enlarged view in Fig. 2(b), only oxides containing toxic elements such as Hg_2WO_4 and As_2PbO_6 are excluded.

Previously identified oxides are also present in Fig. 2(b), but some of them are screened out by the presence of type-3 oxygen vacancies. An example is Ba_2TaBiO_6. Bhatia et al. [12] reported that Ba_2TaBiO_6 has high visible-light transmittance and hole mobility larger than 30 $cm^2/(V\ s)$. However, the hole concentration only reaches 10^{14} cm^{-3} even with a large amount of K doping. The authors attribute this to the strong compensation by donors, such as oxygen vacancies. This illustrates the usefulness of $E_f[V_O]$ as a screening parameter.

As shown in Fig. 2(d), the oxides with Be, B, Mg, Al, and Si oxides tend to have large optical gaps, but they tend to have type-3 oxygen vacancies as shown in Fig. 2(c). Such conflicting trend indicates the difficulty in finding the p-type TCOs.

The fundamental band gaps, optical gaps, and m_h^* values of the seven oxides with small m_h^* values and optical gaps larger than 2.8 eV are listed in Table 1, along with those of $CuAlO_2$ calculated in this study. Na_3AgO_2, $Rb_2Pb_2O_3$, $Cs_2Pb_2O_3$, and Ba_3BAsO_3 are identified as potential *p*-type TCOs. $K_2Pb_2O_3$ and B_6O were proposed by Hautier et al. [8]. Yim et al. have identified CsCuO, but they have not calculated the defect properties. The point defects in B_6O have been thoroughly studied, but it may be difficult to control the hole concentration in B_6O because the acceptor-type defects have large formation energies [60].

The crystal and electronic structures of $Rb_2Pb_2O_3$ and $Cs_2Pb_2O_3$ are almost identical to those of $K_2Pb_2O_3$ (see Table 1 and Fig. S6 in the Supporting Information). Because Ba_3BAsO_3 contains highly toxic As, its commercial use would be extremely difficult. Therefore, the details of Na_3AgO_2, CsCuO, and $K_2Pb_2O_3$, including the defect formation energies calculated using the dd hybrid functionals, are discussed in the following sections.

Table 1. Fundamental band gaps, optical gaps, and hole effective masses in the *x*, *y*, and *z* directions calculated using the dd hybrid functionals for the screened *p*-type TCOs along with those of $CuAlO_2$ for comparison. The space groups of the crystal structures and exact exchange mixing parameters *a* are also given. The bold numbers indicate hole masses below $1.0m_0$, where m_0 is the free-electron rest mass. See the crystal structures in Figs. 3(a), 5(a), and 7(a) for the crystal orientations.

	Space group	*a*	Fundamental band gap (eV)	Optical gap (eV)	$\boldsymbol{m_{h,x}^*}$ (m_0)	$\boldsymbol{m_{h,y}^*}$ (m_0)	$\boldsymbol{m_{h,z}^*}$ (m_0)
$CuAlO_2$	$R\bar{3}m$	0.207	3.91	4.46	1.80	1.80	5.59

Na_3AgO_2	*Ibam*	0.250	3.00	4.02	1.22	2.59	**0.39**
CsCuO	*Cmcm*	0.274	3.18	3.29	5.83	3.56	**0.36**
$K_2Pb_2O_3$	$I2_13$	0.193	2.43	3.00	**0.33**	**0.33**	**0.33**
$Rb_2Pb_2O_3$	$I2_13$	0.205	2.87	3.11	**0.36**	**0.36**	**0.36**
$Cs_2Pb_2O_3$	$I2_13$	0.209	2.83	3.05	**0.41**	**0.41**	**0.41**
B_6O	$R\bar{3}m$	0.172	3.02	5.12	**0.58**	**0.58**	**0.58**
Ba_3BAsO_3	$P6_3/mmc$	0.184	2.51	2.94	4.17	4.17	**0.28**

B. Na_3AgO_2

The crystal structure of Na_3AgO_2 [61] is shown in Fig. 3(a) [60]. The Na^+ ions are tetrahedrally coordinated to O^{2-} ions, while the Ag^+ ions are surrounded by two O^{2-} ions. Such dumbbell-type coordination is commonly observed in Cu and Ag oxides with closed 3*d* and 4*d* shells, respectively, as represented by Cu_2O and Ag_2O.

The calculated band structure, Brillouin zone, and optical absorption spectrum of Na_3AgO_2 are shown in Fig. 3(b)–(d). Na_3AgO_2 has an indirect-type band structure, where the VBM and the conduction band minimum (CBM) are located at the X and Γ points, respectively. The difference between the fundamental band gap and the optical gap is 1.0 eV (Fig. 3(d)). As predicted in this study, single crystal Na_3AgO_2 has been reported to exhibit transparency in experiment [61].

The small m_h^* of 0.39 m_0, where m_0 is the free-electron rest mass, manifests only in the X→G_0 direction, which is parallel to k_z. Because the valence band is composed of hybridized Ag-4*d* and O-2*p* orbitals, as shown in the DOS (Fig. 3(e)), the small m_h^* is attributed to the 1D Ag–O bonding in the *z* direction (see Fig. 3(a)).

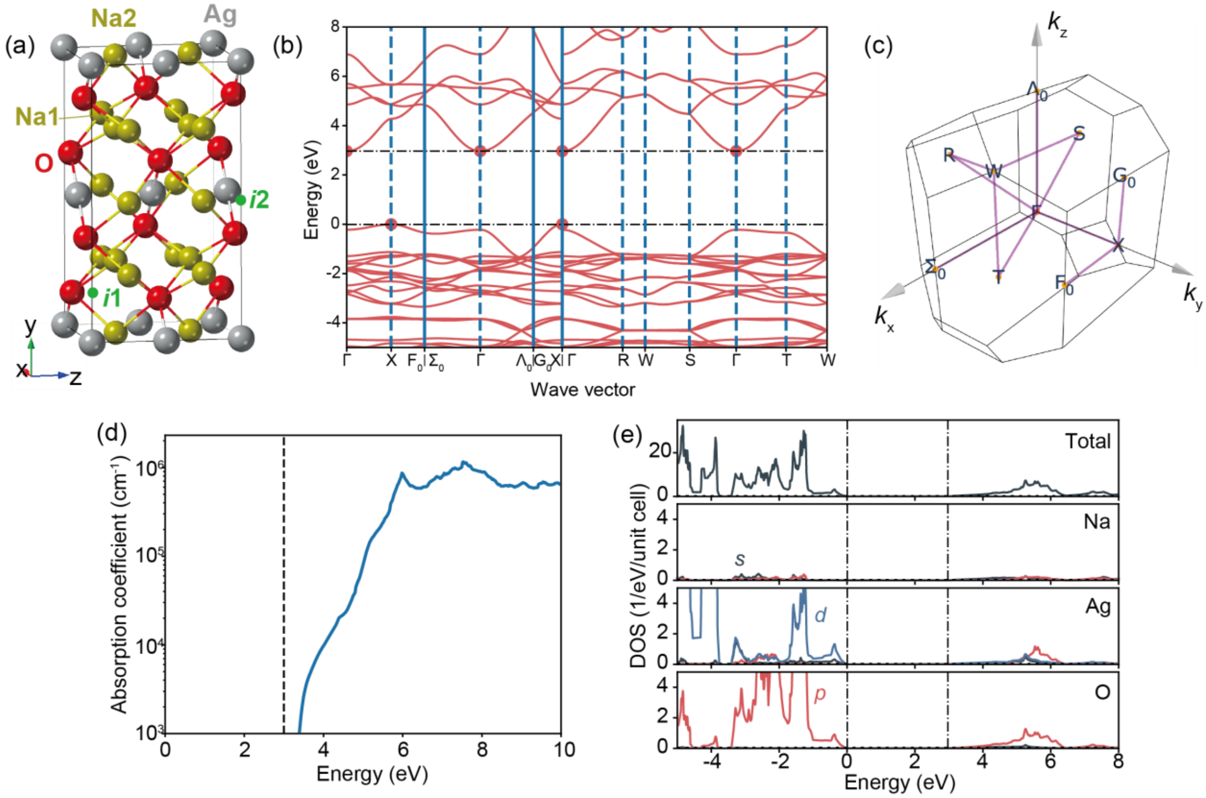

Figure 3. (a) Conventional unit cell, (b) band structure, (c) Brillouin zone, (d) optical absorption spectrum, and (e) total and atom-projected DOS of Na_3AgO_2. In (a), the interstitial sites *i*1 and *i*2 are also shown as small green spheres, which are located at (0.3125, 0.1597, 0.0625) and (0, 0.5, 0) in fractional coordinates, respectively. The inequivalent Na sites are distinguished. The band path in (b) is drawn with purple lines in (c). The atom-projected DOS were obtained by summing the DOS for the same element in the primitive unit cell.

Because the hybridization between the Ag-4*d* and O-2*p* orbitals pushes up the VBM, *p*-type dopability is expected [7]. The Na-Ag-O chemical potential diagram and the defect formation energies in $\mathrm{Na_3AgO_2}$ under the oxygen-rich condition are shown in Fig. 4. Although the oxygen vacancies are doubly positively charged at the VBM, $E_{\mathrm{f}}[V_{\mathrm{O}}]$ is sufficiently large to not compensate for the holes. The cation antisites ($\mathrm{Na_{Ag}}$ and $\mathrm{Ag_{Na}}$) are in the neutral charge state, while the cation vacancies (V_{Na} and V_{Ag}) act as acceptors up to $\Delta\varepsilon_{\mathrm{F}} \approx 0.5$. The split-type Ag vacancy ($V_{\mathrm{Ag(split)}}$) and the split-type Na-on-Ag antisite ($\mathrm{Na_{2Ag(split)}}$) act as acceptors, but they have larger formation energies than those of the vacancies and antisites. All the interstitials have relatively larger formation energies. Two different sites, shown in Fig. 4(a), were calculated for each interstitial. While Ag and O interstitials are relaxed to different defect structures (Ag_{ix} and O_{ix}, (x=1, 2)), respectively, Na interstitials (Na_i) was converged to the same structure. In particular, O_{i1} and O_{i2} have very different formation energies and transition levels.

Next, we show the equilibrium Fermi level at the sample growth temperature (T=973K) [61] (Fig. 4(b)). The calculated hole concentration (p) is $1\mathrm{x}10^{16}$ cm^{-3}, where the concentrations (c) of the dominant defects are $c(V_{\mathrm{Na1}}^{-})=1\mathrm{x}10^{16}$ cm^{-3}, $c(\mathrm{Na_{Ag}}^{0})=8\mathrm{x}10^{20}$ cm^{-3}, and $c(\mathrm{Ag_{Na1}}^{0})=2\mathrm{x}10^{17}$ cm^{-3}. However, when the temperature is lowered to 300K, p is reduced to $3\mathrm{x}10^{11}$ cm^{-3} mainly due to the thermodynamical transition of V_{Na1} at $\Delta\varepsilon_{\mathrm{F}}$ =0.55 eV. As shown in the bottom of the Fig. 4(b), when the temperature is decreased, the Fermi level is decreased as long as p is constant. However, when it crosses a transition level of dominant defects, most of the holes are trapped and the Fermi level is pinned near the transition level. Indeed, the concentration of V_{Na1} is redistributed to $c(V_{\mathrm{Na1}}^{-})=5\mathrm{x}10^{13}$ cm^{-3} and $c(V_{\mathrm{Na1}}^{0})=1\mathrm{x}10^{16}$ cm^{-3} at T=300K. The close transition levels also appear in V_{Na2}, V_{Ag}, and $\mathrm{Na_{2Ag(split)}}$.

To study the transition levels, we plot the squared wavefunction of the unoccupied deep state in the calculation of V_{Na1}^{0} in Fig. 4(c). The hole is distributed along an Ag-Ag chain as a 1D polaronic state. Such 1D is also found for $V_{\mathrm{Na2}}^{0,}$ $V_{\mathrm{Ag}}^{0,}$ and $\mathrm{Na_{2Ag(split)}}{}^{0}$. Since the effective mass along this direction is very small (see Table 1), high hole conductivity can be achieved only in this direction if a sufficient number of polarons are introduced.

To introduce more hole polarons, acceptor-type doping is more desirable. Traditionally, acceptor dopants have been ions with a lower valence than the constituent atoms. For oxides, cation doping is more desirable because it can be achieved simply by sintering the oxides with the dopants. However, in the case of *p*-type doping of monovalent cation oxides, there are no oxides consisting of zero valence elements. To overcome this, Matsuzaki et al. [62] proposed to dope isovalent ions with larger ionic radii than the constituent cations. For example, the hole carrier concentration in Cu_2O is increased by doping Na, which has the same valence as copper but a larger size. Thus, as the size mismatch with Cu^+ in the host lattice is increased, these isovalent impurities are preferentially located in interstitial positions to form stable acceptor-like impurity-defect complexes. Because Ag is located in the same column as Cu in the periodic table, the same hole doping strategy can be expected for Ag compounds.

To verify that this doping strategy works well in Na_3AgO_2, we calculated the K dopants. As shown in the Supplementary Fig. 4(b), the K dopants located at the interstitial sites with two Ag vacancies ($K_{2Ag(split)}$) have lower formation energies than $Na_{2Ag(split)}$, but higher than V_{Na1}. Therefore, non-thermal equilibrium doping is more desirable when K is doped.

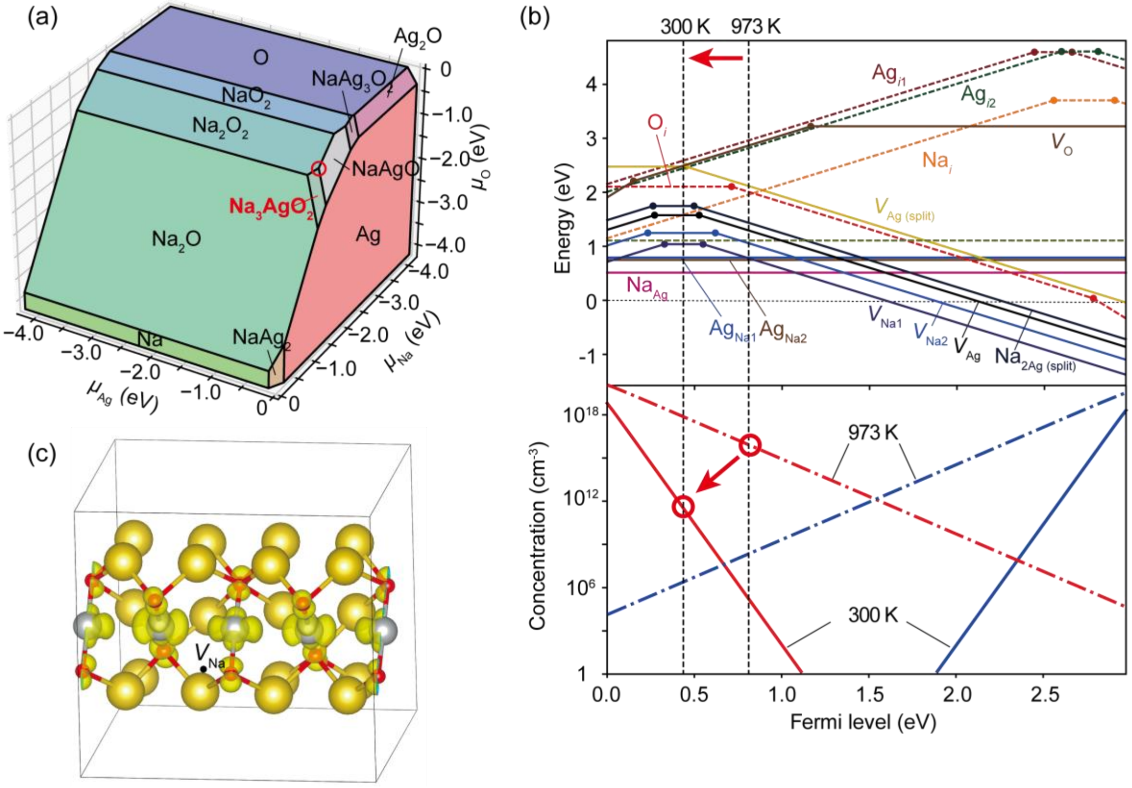

Figure 4. (a) Na-Ag-O chemical potential diagram. (b) Defect formation energies in Na_3AgO_2 under the O-rich condition indicated by the red circle in (a). The K chemical potential is determined from the KAgO total energy. See the text for the definitions of the defect notations. The carrier concentrations at T=973K and 300K are shown at the bottom. The vertical lines indicate the Fermi level (see text for details). The interstitial sites are shown in Fig. 3(a). (c) The squared wavefunction of the unoccupied deep state in the calculation of V_{Na1}^0 drawn using VESTA [63]. The isosurface corresponds to 10% of the maximum value.

C. CsCuO.

The unit cell and electronic structure of CsCuO [61] are shown in Fig. 5. Like Ag^+ in Na_3AgO_2, the Cu^+ ions are coordinated to two O^{2-} ions. The band structure indicates an indirect gap with the VBM located at the Γ point, but the difference between the direct and indirect gaps is negligible. m_h^* is very small ($0.36m_0$) along the $\Gamma \rightarrow Z$ (k_z) direction. The single crystal of CsCuO is also known to exhibit transparency, which is consistent with this study [64].

In the DOS (Fig. 5(e)), the valence bands are composed of hybridized Cu-3d and O-2p orbitals, and thus small m_h^* is attributed to the Cu-O channel along the z direction, as shown in Fig. 5(a), which is similar to Na_3AgO_2.

m_h^* is closely related to the crystal structure. When Cs is replaced by Na, K, or Rb, the structure changes to the $I4/mmm$ phase (see Fig. S4 in the Supporting Information). In this structure, m_h^* increases significantly from $0.36m_0$ to $1.89\text{-}3.21m_0$ because the Cu-O bonding pathway is interrupted by the alkali metal ions. Therefore, the continuous bonding that constitutes the VBM in real space is the key to low m_h^*.

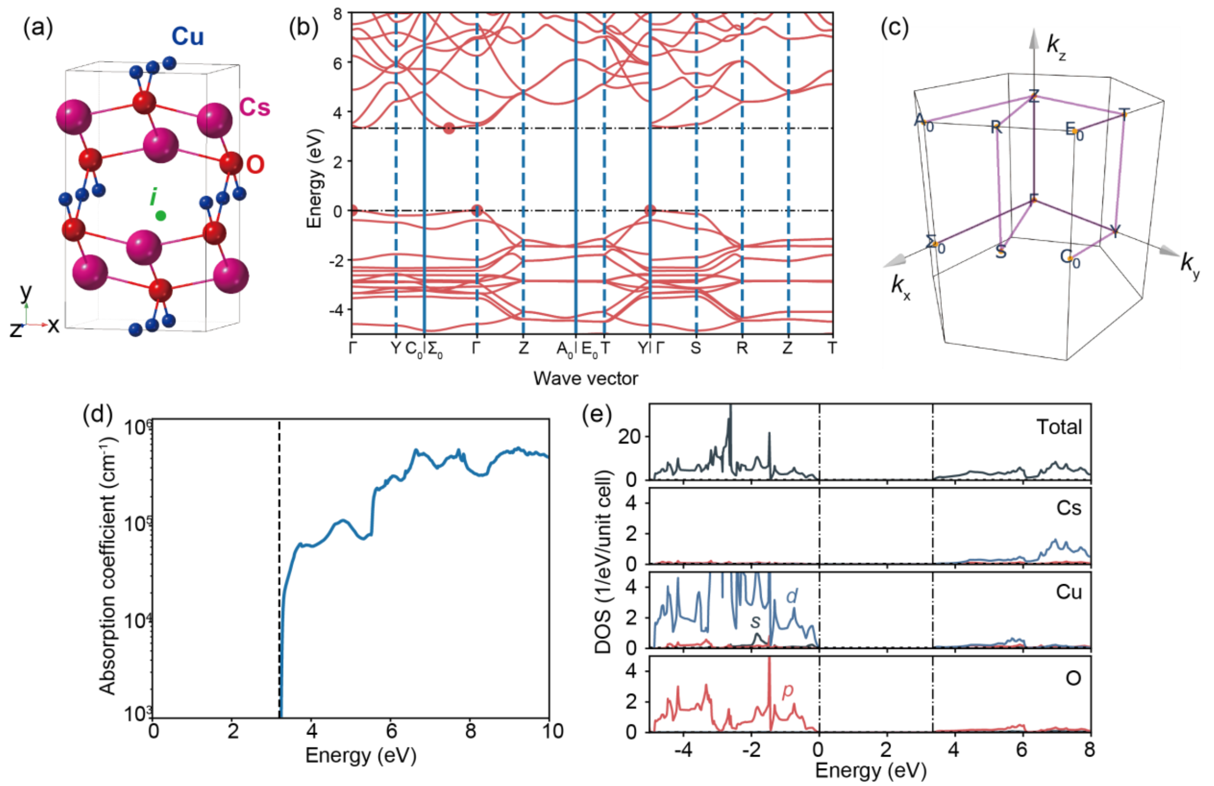

Figure 5. (a) Conventional unit cell, (b) band structure, (c) Brillouin zone, (d) optical absorption spectrum, and (e) total and atom-projected DOS of CsCuO. The interstitial site (*i*) in (a) is located at (0.5, 0.4167, 0.25) in fractional coordinates.

The Cs-Cu-O chemical potential diagram and the defect formation energies in CsCuO under the O-rich condition are shown in Fig. 6. The large area of CsCuO in the chemical potential diagram indicates its high stability with respect to the competing phases. The defect formation energies show a similar tendency to those in Na_3AgO_2. The formation energy of the oxygen vacancy is large even at $\Delta\varepsilon_F = 0$, while the cation vacancies (V_{Cs} and V_{Cu}) act as acceptors with relatively small formation energies (Fig. 6(b)). However, in contrast to Na_3AgO_2, the antisite defects (Cs_{Cu}

and Cu_{Cs}) have large formation energies due to the large ionic size mismatch between Cs and Cu (1.67 Å vs. 0.46 Å in the four-coordination number) [65]. The split-type interstitial ($Cs_{2Cu(split)}$), where Cs is located at the center of two copper vacancies (V_{Cu}), has a larger energy than the cesium vacancy (V_{Cs}) and V_{Cu}. The Cu and O interstitials (Cu_i and O_i) have relatively large formation energies. On the contrary, despite the large ionic size of Cs, the Cs interstitial (Cs_i) is the dominant donor at $\Delta\varepsilon_F$ located near the VBM mainly due to the large voids in the Cs layers (see Fig. 5(a)).

The equilibrium Fermi levels at T=673K and 300K are also shown in Fig. 6(b). Although the equilibrium hole concentration at 673K is $5\text{x}10^{15}$ cm^{-3}, which is mainly caused by V_{Cs}^{-1}, it is largely reduced to $4\text{x}10^{10}$ cm^{-3} at 300K as in Na_3AgO_2. To understand the origin of the deep state, we plot the squared wavefunction of the unoccupied deep state in the calculation of $V_{Cs}{}^{0}$ and $V_{Cu}{}^{0}$ in Figs. 6(c) and (d). It is found that a 1D polaronic state exists near $V_{Cs}{}^{0}$, while a small polaron is distributed at the Cu and O sites near the Cu vacancy. The difference would be mainly because the 1D Cu-Cu structure is broken by $V_{Cu}{}^{0}$. If the small polaronic states are dominant, it would be difficult to introduce carrier holes even with *p*-type doping.

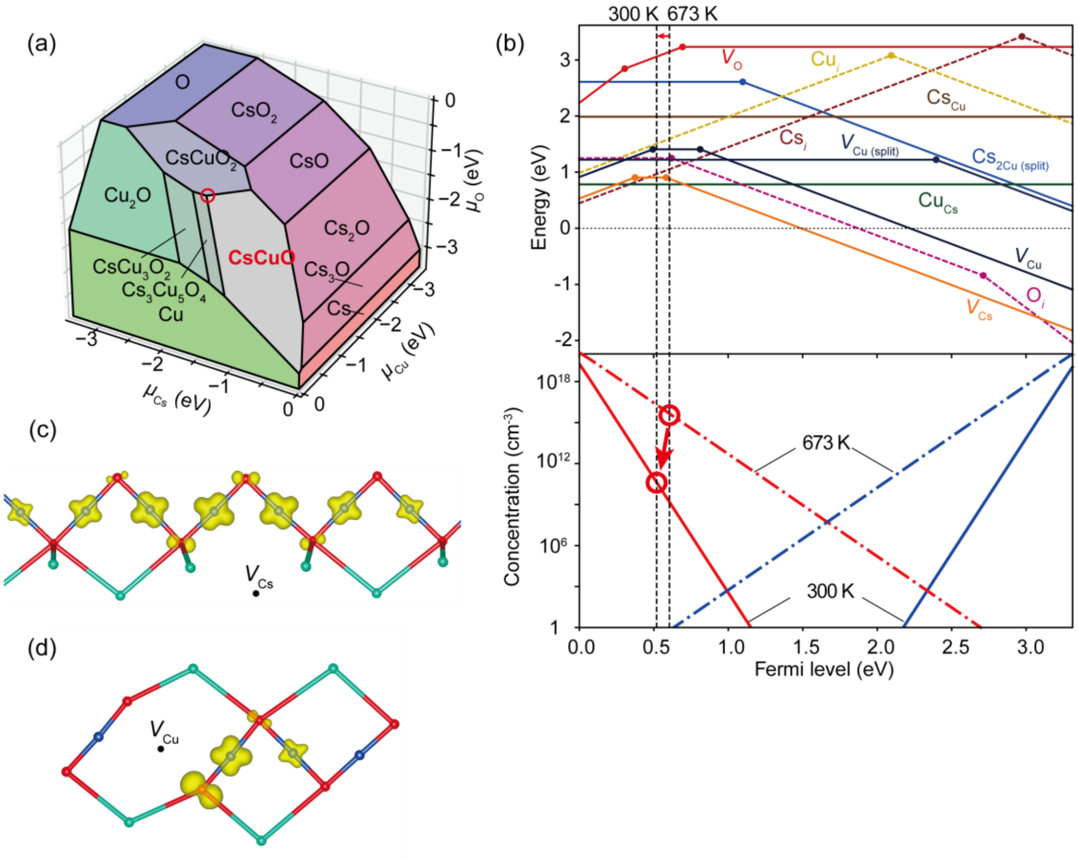

Figure 6. (a) Cs-Cu-O chemical potential diagram. (b) Defect formation energies in CsCuO under the O-rich condition indicated by the red circle in (a). The interstitial site is shown in Fig. 5(a). (c, d) The squared wavefunction of unoccupied deep state in the calculation of (c) $V_{\mathrm{Cs}}{}^{0}$ and (d) $V_{\mathrm{Cu}}{}^{0}$. The isosurfaces correspond to 10% of their respective maxima.

D. $K_2Pb_2O_3$.

The crystal structure, band structure, optical absorption spectrum, and DOS of $K_2Pb_2O_3$ are shown in Fig. 7. The $6s^2$ lone-pair electrons of the Pb^{2+} ions in $K_2Pb_2O_3$ point to the free space (see Fig. S5 in the Supporting Information for the electron localization function) [66]. $K_2Pb_2O_3$ also has an indirect-type band structure with the VBM at the H point. The valence band is mainly composed of hybridized Pb-6s and O-2p orbitals. Unlike Na_3AgO_2 and CsCuO, $K_2Pb_2O_3$ has a small m_h^* in all directions because of the three-dimensional Pb-O network.

Experimentally, single crystal $K_2Pb_2O_3$ with ø=5mm was reported to be clearly transparent with orange color [67]. It is difficult to explain the origin of the color, but if it is caused by the defects, such coloration can be reduced by changing the growth condition, so experimental verification is highly desirable.

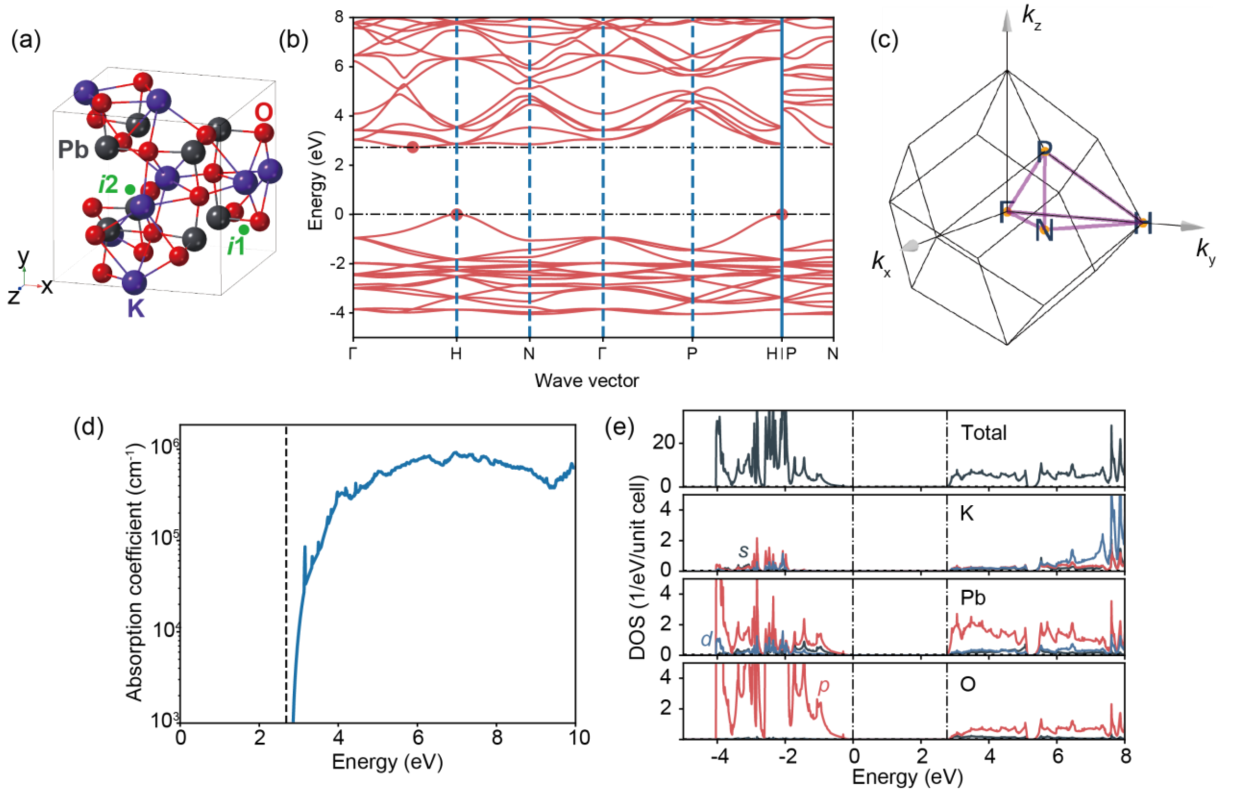

Figure 7. (a) Conventional unit cell, (b) band structure, (c) Brillouin zone, (d) optical absorption spectrum, and (e) total and atom-projected DOS of $K_2Pb_2O_3$. The interstitial sites *i*1 and *i*2 in (a) are located at (0.9948, 0.2691, 0.5556) and (0.3009, 0.4398, 0.5185) in fractional coordinates, respectively.

The K-Pb-O chemical potential diagram and defect formation energies in $K_2Pb_2O_3$ under the O-rich condition are shown in Fig. 8. The vacancy properties are similar to those of Na_3AgO_2 and CsCuO. The oxygen vacancies have large formation energies, while the cation vacancies (V_{Pb} and V_K) act as acceptors with relatively small formation energies. In contrast, because K and Pb have different oxidation states, K-on-Pb (K_{Pb}) and Pb-on-K (Pb_K) act as a single acceptor and a single donor, respectively, in the *p*-type region. We calculated two different sites for each interstitial, as shown in Fig. 7(a), but have found that they are relaxed to the same defect structure. The cation interstitials (K_i and Pb_i) act as deep donors with relatively large formation energies, while the oxygen interstitials (O_i) act as shallow acceptors with formation energies comparable to those of the other dominant acceptors.

Hautier et al. [8] also identified $K_2Pb_2O_3$ as a promising *p*-type TCO, and they calculated the vacancies (V_O, V_{Pb}, and V_K) using the PBE functional with band-edge corrections in the G_0W_0 approximation. Our calculated vacancy formation energies are similar to their results, but the −1/−2 and −2/−4 transition levels of V_{Pb} in Ref. [8] do not appear in our calculations.

To verify the hole doping by impurities, we calculated the defect formation energies of Na dopants because the ionic radius of Na^+ (1.16Å in the six-coordinate [65]) is closer to that of Pb^{2+} (1.33 Å) than to that of K^+ (1.52 Å). As shown in Fig. 8(b), in the *p*-type regime, although the Na impurities are mainly located at the K sites in the neutral charge states, they also exist in the negatively charged state at the Pb site (Na_{Pb}). Because Na_{Pb}^- has a larger formation energy, non-thermal equilibrium doping is desired for further hole doping.

Our screening also identified $Rb_2Pb_2O_3$ and $Cs_2Pb_2O_3$ as potential *p*-type TCOs, which are isostructural to $K_2Pb_2O_3$. In fact, their electronic structures and band gaps are almost identical (Table 1 and Fig. S6 in the Supporting Information). The disadvantage of $A_2Pb_2O_3$ (A = K, Rb, Cs) is that they contain toxic Pb ions. Unfortunately, replacing Pb with Sn reduces the band gaps to values unsuitable for TCs [8].

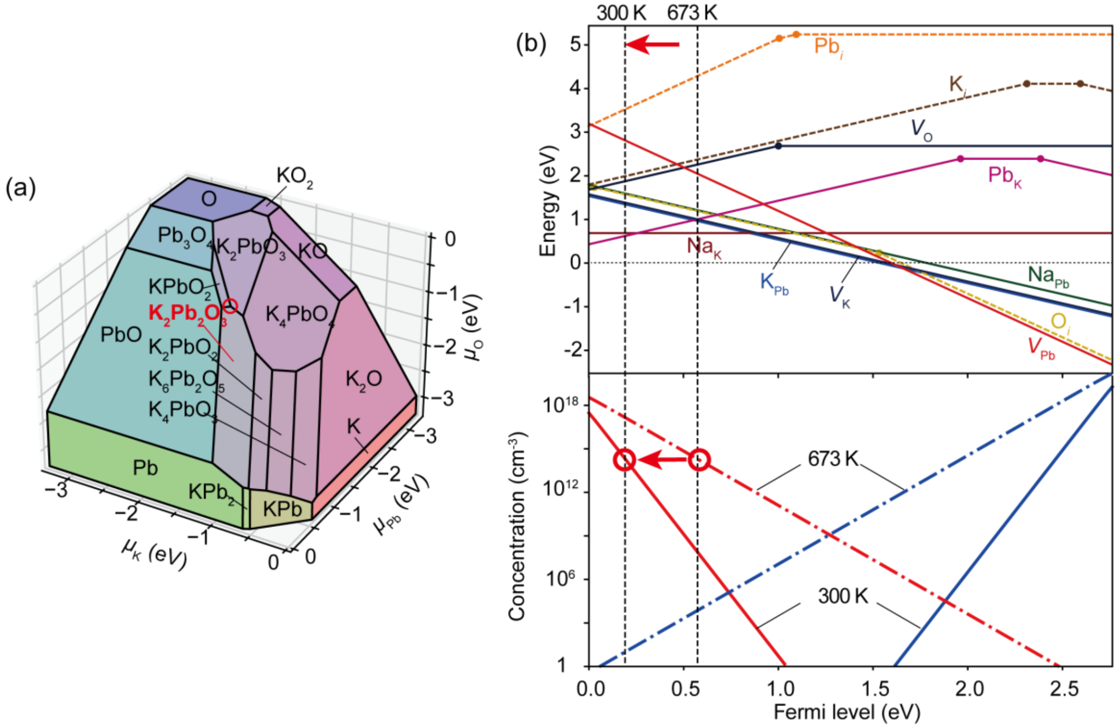

Figure 8. (a) K-Pb-O chemical potential diagram. (b) Defect formation energies in $K_2Pb_2O_3$ under the O-rich condition designated in (a). The Na chemical potential is determined from the Na_2PbO_3 total energy. The formation energies of the Na dopant are also shown. The interstitial sites are shown in Fig. 7(a).

Although CsCuO and $K_2Pb_2O_3$ have been previously proposed as potential *p*-type TCOs, respectively [8], they have not attracted much attention [9]. This is partly because the band gaps of CsCuO and $K_2Pb_2O_3$ calculated by the HSE functional and the GW_0 approximation, respectively, are 2.45 and 2.6 eV, which are smaller than the desirable gap of 3.1 eV. However, it should be kept in mind that accurate prediction of the band gap is generally not an easy task [11] even using high-level approximations. For example, the calculated band gap of Ba_2TaBiO_6 using the G_0W_0 approximation is 3.8 eV, while the experimental gap is reported to range between 3.2 -- 5.0

eV [12,68]. Therefore, experimental verification is essential to determine whether the screened oxides truly exhibit high performance as *p*-type TCOs.

IV. Discussion and conclusions

We have screened potential *p*-type TCOs using the optical absorption spectra and effective masses calculated with accurate dd hybrid functionals and the formation energies of oxygen vacancies, which are the main hole killers in oxides. Consequently, we identified six potential *p*-type TCOs. Na_3AgO_2 was identified as a potential *p*-type TCO, while the previously proposed *p*-type TCOs CsCuO, $K_2Pb_2O_3$, and B_6O were also identified. $Rb_2Pb_2O_3$ and $Cs_2Pb_2O_3$ were identified as *p*-type TCOs, but they were found to have almost identical properties to $K_2Pb_2O_3$. For Na_3AgO_2, CsCuO, and $K_2Pb_2O_3$, we calculated the vacancies, antisites, and interstitials using dd hybrid functionals. They are predicted to be *p*-type semiconductors even without external doping.

Many of the previously proposed *p*-type TCOs have been rediscovered in this study, indicating that previous screening studies work satisfactorily. However, we would like to emphasize that the importance of our screening is that it allows us to remove a large fraction of inappropriate oxides based on $E_f[V_O]$. Indeed, only 156 out of the 845 oxides were found to have benign oxygen vacancies for *p*-type doping. Eliminating such false-positive candidates should increase the success rate of finding *p*-type TCOs in labor-intensive experiments.

We would like to emphasize that although the *p*-type TCOs have been screened based on the formation energies of oxygen vacancies, it is essential to calculate all possible point defects for the screened candidates for the following reasons. First, other hole killers may be present. In particular, cation antisites are very likely in oxides composed of two or more cations. Second, to achieve the *p*-type doping, we need to know the formation energies of acceptor type defects and acceptor dopants. Indeed, we found that Na_3AgO_2 and CsCuO exhibit the 1D polaronic behavior, which would prevent high conductivity in three dimensional directions. Furthermore, it is preferable to perform these calculations at the hybrid functional level to increase the predictive power.

We also note that some research has shown that hydrogen passivation with hole killer defects can avoid the incorporation of oxygen vacancies [69]. This technique, in fact, has been successfully used to obtain *p*-type gallium nitrides [70]. Therefore, the rejected oxides in this study should not be completely dismissed for future consideration.

In the future, the accuracy of the band gaps will be improved and the optical absorption spectra and point-defect formation energies will be published in publicly available computational databases, such as the Materials Project database [21]. This study serves as a good example of the use of these datasets. In addition, our calculated optical absorption spectra, band structures, and effective masses, which are available in the GitHub repository [71], will also be useful for screening other classes of materials, such as solar-cell absorbates and light-emitting diodes.

ACKNOWLEDGMENTS

We greatly appreciate S. Iimura and K. Matsuzaki for fruitful discussion. This study was financially supported by PRESTO (JPMJPR16N4) from the Japan Science and Technology Agency, KAKENHI (Grant No. 22H01755), and the E-IMR project at IMR, Tohoku University.

REFERENCES

[1] A. Stadler, *Transparent Conducting Oxides—An Up-To-Date Overview*, Materials 5, 661 (2012).

[2] H. Hosono, *Transparent Oxide Semiconductors: Fundamentals and Recent Progress* (John Wiley & Sons, Ltd, 2010).

[3] T. Minami, *Present Status of Transparent Conducting Oxide Thin-Film Development for Indium-Tin-Oxide (ITO) Substitutes*, Thin Solid Films 516, 5822 (2008).

[4] K. Nomura, H. Ohta, A. Takagi, T. Kamiya, M. Hirano, and H. Hosono, *Room-Temperature Fabrication of Transparent Flexible Thin-Film Transistors Using Amorphous Oxide Semiconductors*, Nature 432, 488 (2004).

[5] K. H. L. Zhang, K. Xi, M. G. Blamire, and R. G. Egdell, *P-Type Transparent Conducting Oxides*, Journal of Physics: Condensed Matter 28, 383002 (2016).

[6] X. Cai and S.-H. Wei, *Perspective on the Band Structure Engineering and Doping Control of Transparent Conducting Materials*, Appl Phys Lett 119, 070502 (2021).

[7] H. Kawazoe, M. Yasukawa, H. Hyodo, M. Kurita, H. Yanagi, and H. Hosono, *P-Type Electrical Conduction in Transparent Thin Films of CuAlO2*, Nature 389, 939 (1997).

[8] G. Hautier, A. Miglio, G. Ceder, G.-M. Rignanese, and X. Gonze, *Identification and Design Principles of Low Hole Effective Mass P-Type Transparent Conducting Oxides*, Nature Communications 4, 2292 (2013).

[9] K. Yim, Y. Youn, M. Lee, D. Yoo, J. Lee, S. H. Cho, and S. Han, *Computational Discovery of P-Type Transparent Oxide Semiconductors Using Hydrogen Descriptor*, Npj Comput Mater 4, 17 (2018).

[10] J. B. Varley, A. Miglio, V.-A. Ha, M. J. van Setten, G.-M. Rignanese, and G. Hautier, *High-Throughput Design of Non-Oxide P-Type Transparent Conducting Materials: Data Mining, Search Strategy, and Identification of Boron Phosphide*, Chem Mater 29, 2568 (2017).

[11] R. Woods-Robinson, D. Broberg, A. Faghaninia, A. Jain, S. S. Dwaraknath, and K. A. Persson, *Assessing High-Throughput Descriptors for Prediction of Transparent Conductors*, Chemistry of Materials 30, 8375 (2018).

[12] A. Bhatia et al., *High-Mobility Bismuth-Based Transparent p-Type Oxide from High-Throughput Material Screening*, Chemistry of Materials 28, 30 (2015).

[13] H. Peng et al., *Li-Doped Cr2MnO4: A New P-Type Transparent Conducting Oxide by Computational Materials Design*, Adv Funct Mater 23, 5267 (2013).

[14] N. Sarmadian, R. Saniz, B. Partoens, and D. Lamoen, *Easily Doped P-Type, Low Hole Effective Mass, Transparent Oxides*, Sci Rep-Uk 6, 20446 (2016).

[15] B. A. D. Williamson, J. Buckeridge, J. Brown, S. Ansbro, R. G. Palgrave, and D. O. Scanlon, *Engineering Valence Band Dispersion for High Mobility P-Type Semiconductors*, Chem Mater 29, 2402 (2017).

[16] J. P. Perdew, K. Burke, and M. Ernzerhof, *Generalized Gradient Approximation Made Simple*, Phys Rev Lett 77, 3865 (1996).

[17] L. Hedin, *New Method for Calculating the One-Particle Green's Function with Application to the Electron-Gas Problem*, Phys Rev 139, A796 (1965).

[18] A. Walsh et al., *Nature of the Band Gap of In2O3 Revealed by First-Principles Calculations and X-Ray Spectroscopy*, Physical Review Letters 100, 167402 (2008).

[19] X. Cai, P. Zhang, and S.-H. Wei, *Revisit of the Band Gaps of Rutile SnO2 and TiO2: A First-Principles Study*, J Semicond 40, 092101 (2019).

[20] X. Nie, S.-H. Wei, and S. B. Zhang, *Bipolar Doping and Band-Gap Anomalies in Delafossite Transparent Conductive Oxides*, Phys Rev Lett 88, 066405 (2002).

[21] A. Jain et al., *Commentary: The Materials Project: A Materials Genome Approach to Accelerating Materials Innovation*, APL MATERIALS 1, 011002 (2013).

[22] F. K. Shan and Y. S. Yu, *Band Gap Energy of Pure and Al-Doped ZnO Thin Films*, J Eur Ceram Soc 24, 1869 (2004).

[23] M. Balog, M. Schieber, M. Michman, and S. Patai, *The Chemical Vapour Deposition and Characterization of ZrO2 Films from Organometallic Compounds*, Thin Solid Films 47, 109 (1977).

[24] P. Y. Yu and M. Cardona, *Fundamentals of Semiconductors Physics and Materials Properties*, Fourth Edition (Springer, 2010).

[25] S. Ponc, W. Li, S. Reichardt, and F. Giustino, *First-Principles Calculations of Charge Carrier Mobility and Conductivity in Bulk Semiconductors and Two-Dimensional Materials*, Rep Prog Phys 83, 036501 (2020).

[26] S. Zhang, S. H. Wei, and A. Zunger, *Intrinsic N-Type versus p-Type Doping Asymmetry and the Defect Physics of ZnO*, Physical Review B 63, 075205 (2001).

[27] P. Ágoston and K. Albe, *Intrinsic N-Type Behavior in Transparent Conducting Oxides: A Comparative Hybrid-Functional Study of In_{2}O_{3}, SnO_{2}, and ZnO*, Physical Review Letters 103, 245501 (2009).

[28] N. Tsunoda, Y. Kumagai, and F. Oba, *Stabilization of Small Polarons in BaTiO3 by Local Distortions*, Physical Review Materials 3, 114602 (2019).

[29] M. Choi, F. Oba, Y. Kumagai, and I. Tanaka, *Anti-ferrodistortive-Like Oxygen-Octahedron Rotation Induced by the Oxygen Vacancy in Cubic SrTiO3*, Advanced Materials 25, 86 (2013).

[30] Y. Kumagai, N. Tsunoda, A. Takahashi, and F. Oba, *Insights into Oxygen Vacancies from High-Throughput First-Principles Calculations*, Phys Rev Mater 5, 123803 (2021).

[31] J. H. Skone, M. Govoni, and G. Galli, *Self-Consistent Hybrid Functional for Condensed Systems*, Physical Review B 89, 195112 (2014).

[32] P. E. Blöchl, *Projector Augmented-Wave Method*, Physical Review B 50, 17953 (1994).

[33] G. Kresse and D. Joubert, *From Ultrasoft Pseudopotentials to the Projector Augmented-Wave Method*, Phys Rev B 59, 1758 (1999).

[34] G. Kresse and J. Furthmüller, *Efficient Iterative Schemes for Ab Initio Total-Energy Calculations Using a Plane-Wave Basis Set*, Phys Rev B 54, 11169 (1996).

[35] J. P. Perdew, A. Ruzsinszky, G. I. Csonka, O. A. Vydrov, G. E. Scuseria, L. A. Constantin, X. Zhou, and K. Burke, *Restoring the Density-Gradient Expansion for Exchange in Solids and Surfaces*, Phys Rev Lett 100, 136406 (2008).

[36] S. L. Dudarev, S. Y. Savrasov, C. J. Humphreys, and A. P. Sutton, *Electron-Energy-Loss Spectra and the Structural Stability of Nickel Oxide: An LSDA+U Study*, Phys. Rev. B 57, 1505 (1998).

[37] Y. Hinuma, G. Pizzi, Y. Kumagai, F. Oba, and I. Tanaka, *Band Structure Diagram Paths Based on Crystallography*, Computational Materials Science 128, 140 (2017).

[38] G. K. H. Madsen, J. Carrete, and M. J. Verstraete, *BoltzTraP2, a Program for Interpolating Band Structures and Calculating Semi-Classical Transport Coefficients*, Computer Physics Communications 231, 140 (2018).

[39] Y. Kumagai, *vise*, https://github.com/kumagai-group/vise.

[40] A. Jain et al., *FireWorks: A Dynamic Workflow System Designed for High-throughput Applications*, Concurrency and Computation: Practice and Experience 27, 5037 (2015).

[41] S. P. Ong, W. D. Richards, A. Jain, G. Hautier, M. Kocher, S. Cholia, D. Gunter, V. L. Chevrier, K. A. Persson, and G. Ceder, *Python Materials Genomics (Pymatgen): A Robust, Open-Source Python Library for Materials Analysis*, Computational Materials Science 68, 314 (2013).

[42] Y. Hinuma, Y. Kumagai, I. Tanaka, and F. Oba, *Band Alignment of Semiconductors and Insulators Using Dielectric-Dependent Hybrid Functionals: Toward High-Throughput Evaluation*, Physical Review B 95, 075302 (2017).

[43] S. van der Walt, J. L. Schönberger, J. Nunez-Iglesias, F. Boulogne, J. D. Warner, N. Yager, E. Gouillart, T. Yu, and scikit-image contributors, *Scikit-Image: Image Processing in Python*, Peerj 2, e453 (2014).

[44] A. F. Wright and J. S. Nelson, *Theory of the Copper Vacancy in Cuprous Oxide*, J Appl Phys 92, 5849 (2002).

[45] Y. Kumagai, L. A. Burton, A. Walsh, and F. Oba, *Electronic Structure and Defect Physics of Tin Sulfides: SnS, , Sn2S3 , and SnS2*, Physical Review Applied 6, 014009 (2016).

[46] Y. Kumagai and F. Oba, *Electrostatics-Based Finite-Size Corrections for First-Principles Point Defect Calculations*, Phys. Rev. B 89, 195205 (2014).

[47] C. Freysoldt, J. Neugebauer, and C. V. de Walle, *Fully Ab Initio Finite-Size Corrections for Charged-Defect Supercell Calculations*, Physical Review Letters 102, 016402 (2009).

[48] Y. Kumagai, K. Harada, H. Akamatsu, K. Matsuzaki, and F. Oba, *Carrier-Induced Band-Gap Variation and Point Defects in Zn3N2 from First Principles*, Phys Rev Appl 8, 014015 (2017).

[49] Y. Kumagai, M. Choi, Y. Nose, and F. Oba, *First-Principles Study of Point Defects in Chalcopyrite ZnSnP2*, Physical Review B 90, 125202 (2014).

[50] T. Gake, Y. Kumagai, and F. Oba, *First-Principles Study of Self-Trapped Holes and Acceptor Impurities in Ga2O3 Polymorphs*, Physical Review Materials 3, 044603 (2019).

[51] N. Tsunoda, Y. Kumagai, M. Araki, and F. Oba, *One-Dimensionally Extended Oxygen Vacancy States in Perovskite Oxides*, Physical Review B 99, 060103 (2019).

[52] N. Tsunoda, Y. Kumagai, A. Takahashi, and F. Oba, *Electrically Benign Defect Behavior in Zinc Tin Nitride Revealed from First Principles*, Physical Review Applied 10, 011001 (2018).

[53] Y. Kumagai, N. Tsunoda, and F. Oba, *Point Defects and P-Type Doping in ScN from First Principles*, Physical Review Applied 9, 034019 (2018).

[54] A. Wang, R. Kingsbury, M. McDermott, M. Horton, A. Jain, S. P. Ong, S. Dwaraknath, and K. A. Persson, *A Framework for Quantifying Uncertainty in DFT Energy Corrections*, Sci Rep-Uk 11, 15496 (2021).

[55] Y. Kumagai, *pydefect*, https://github.com/kumagai-group/pydefect.

[56] S. Lany, J. Osorio-Guillén, and A. Zunger, *Origins of the Doping Asymmetry in Oxides: Hole Doping in NiO versus Electron Doping in ZnO*, Phys Rev B 75, 241203 (2007).

[57] A. Goyal and V. Stevanović, *Metastable Rocksalt ZnO Is P-Type Dopable*, Phys Rev Mater 2, 084603 (2018).

[58] Y. Ogo, H. Hiramatsu, K. Nomura, H. Yanagi, T. Kamiya, M. Hirano, and H. Hosono, *P-Channel Thin-Film Transistor Using p-Type Oxide Semiconductor, SnO*, Applied Physics Letters 93, 032113 (2008).

[59] See Supplemental Material at [URL will be inserted by publisher] for evaluation of the accuracy of the dd hybrid functional, screening results with different criterion, K impurity energies in Na_3AgO_2, band structures of NaCuO, KCuO, and RbCuO, electron localization function in $K_2Pb_2O_3$, and band structures of $Rb_2Pb_2O_3$ and $Cs_2Pb_2O_3$.

[60] J. B. Varley, V. Lordi, A. Miglio, and G. Hautier, *Electronic Structure and Defect Properties of B6O from Hybrid Functional and Many-Body Perturbation Theory Calculations: A Possible Ambipolar Transparent Conductor*, Physical Review B 90, 045205 (2014).

[61] H. Klassen and R. Hoppe, *Alkalioxoargentate(I). Über Na3AgO2*, Zeitschrift Für Anorganische Und Allgemeine Chemie 485, 92 (1982).

[62] K. Matsuzaki, N. Tsunoda, Y. Kumagai, Y. Tang, K. Nomura, F. Oba, and H. Hosono, *Hole-Doping to a Cu(I)-Based Semiconductor with an Isovalent Cation: Utilizing a Complex Defect as a Shallow Acceptor*, J Am Chem Soc 144, 16572 (2022).

[63] K. Momma and F. Izumi, *VESTA 3 for Three-Dimensional Visualization of Crystal, Volumetric and Morphology Data*, J Appl Crystallogr 44, 1272 (2011).

[64] H. Klassen and R. Hoppe, *Neue Oxocuprate(I): Zur Kenntnis von CsCuO*, Zeitschrift Für Anorganische Und Allgemeine Chemie 497, 70 (1983).

[65] R. D. Shannon, *Revised Effective Ionic Radii and Systematic Studies of Interatomic Distances in Halides and Chalcogenides*, Acta Crystallographica Section A 32, 751 (1976).

[66] B. Silvi and A. Savin, *Classification of Chemical Bonds Based on Topological Analysis of Electron Localization Functions*, Nature 371, 683 (1994).

[67] K. -P. Martens and R. Hoppe, *Zum System K2O/PbO. Zur Kenntnis von K2Pb2O3*, Zeitschrift Für Anorganische Und Allgemeine Chemie 437, 116 (2010).

[68] J. Shi et al., *Modulation of the Bi3+ 6s2 Lone Pair State in Perovskites for High-Mobility P-Type Oxide Semiconductors*, Adv Sci 9, 2104141 (2022).

[69] S. Chae et al., *Toward the Predictive Discovery of Ambipolarly Dopable Ultra–Wide–Band–Gap Semiconductors: The Case of Rutile GeO2*, Appl Phys Lett 118, 260501 (2021).

[70] S. Nakamura, N. Iwasa, M. S. M. Senoh, and T. M. T. Mukai, *Hole Compensation Mechanism of P–Type GaN Films*, Jpn J Appl Phys 31, 1258 (1992).

[71] Y. Kumagai, https://github.com/yuuukuma/p_tco_2023.